Nanoscale

Imaging of intracellular protein aggregates through plasmon-assisted clusteroluminescence

Journal:	*Nanoscale*
Manuscript ID	NR-ART-04-2024-001803
Article Type:	Paper
Date Submitted by the Author:	25-Apr-2024
Complete List of Authors:	Dhillon, Ashish Kumar; Indian Institute of Technology Delhi, Department of Chemistry Dudhe, Pranay; Regional Centre for Biotechnology Majumdar, Shubhangi; Indian Institute of Technology Delhi, Chemistry Barman, Sanmitra; BML Munjal University Ghosh, Dibyajyoti; Indian Institute of Technology Delhi, Chemistry Dhanasekaran, Karthigeyan ; Regional Centre for Biotechnology, Centrosome and Cilia Laboratory Siddhanta, Soumik ; Indian Institute of Technology Delhi,

ARTICLE

Imaging of intracellular protein aggregates through plasmon-assisted clusteroluminescence

Received 00th January 20xx,
Accepted 00th January 20xx

DOI: 10.1039/x0xx00000x

Ashish Kumar Dhillon,[a] Pranay Eknath Dudhe,[b] Shubhangi Majumdar,[a] Sanmitra Barman,[c] Dibyajyoti Ghosh,[a,d*] Karthigeyan Dhanasekaran,[b*] and Soumik Siddhanta [a*]

The formation of clusters in non-aromatic molecules can give rise to unconventional luminescence or clusteroluminescence. Typically containing heteroatoms without extended conjugation or aromatic rings, these molecules have drawn much attention owing to the prospects of label-free biological imaging. However, their applications have been limited due to the lack of knowledge of the underlying mechanism. Herein, we have elucidated the mechanism of clusteroluminescence from proteins, which were explicitly aggregated using plasmonic silver nanoparticles. The nanoparticles promoted protein aggregation and induced nitrile formation on the surface, which, along with other lone-pair-containing heteroatoms, contributed to the enhanced emission in the visible range. Remarkably, this makes imaging of proteins possible with visible excitations, as co-factor-lacking proteins generally undergo electronic transitions only in the UV range. Furthermore, the inherent protein-aggregating behaviour of plasmonic nanoparticles was harnessed for imaging of intracellular huntingtin protein aggregates overexpressed in HeLa cells through clusteroluminescence. Significant plasmon-enhanced and red-shifted fluorescence emission was observed, which helped in the imaging and localizing of the intra-cellular aggregates. Density functional theory calculations and transient absorbance spectroscopy were used to probe the molecular interactions at the protein-nanoparticle interface and the charge transfer states, further elucidating the role of nanoparticles and the emission mechanism. This technique thus opens alternate avenues for label-free fluorescence bioimaging.

1. Introduction

Imaging of biological entities is crucial in understanding critical and complex diseases, and optical and spectroscopic modalities have played a central role. Fluorescence emission, light absorbance, vibrational scattering, and nuclear magnetic resonance provide a wealth of molecular information about the biological system.[1-3]This molecular information helps in elucidating the composition, structure, and kinetics of biomolecules which sheds light on the pathogenesis of diseases, specifically neurodegenerative ones. Optical techniques such as fluorescence or vibrational spectroscopy provide excellent spatial and temporal resolution of biological entities even in their native conditions in the cells. However, exogenous labels or fluorescent tags and dye molecules often used in these techniques can perturb the aggregation kinetics and cause toxicity and aggregation-induced quenching or photobleaching.[4-7] Due to these complexities in detecting and probing protein aggregates, there is an interest in label-free detection and imaging, which can be performed in real-time and under physiological conditions.[3, 8-10]

Intrinsic fluorescence or autofluorescence has been used for biological imaging, as reported in the literature. The intrinsic fluorescence from protein molecules arising from phenylalanine, tyrosine, and tryptophan has enabled the detection of conformational changes and ligand binding events.[11, 12] The recent demonstration that fluorescence can arise even from non-aromatic entities, specifically heteroatom-containing molecules, has opened up the area of unconventional fluorescence.[13, 14] This emission occurs in systems under an aggregated state, indicating through-space interactions. Being classified as clusteroluminogens, the through-space n-n interaction, and through-space n-π-interactions are found to be responsible for the emissions in non-pi conjugated systems.[15] This unconventional fluorescence has been observed in macromolecules such as cellulose and proteins, which possess 'n' or separated non-conjugated 'π' electrons, respectively.[16] A host of natural biological systems also have similar heteroatoms and exhibit unconventional emission properties.[17] Therefore, the cluster-triggered emission has the potential to be used in applications such as imaging of biological systems. However, their utility appears to be severely affected by the requirement of a high concentration of molecules to form clusters and the low quantum yield of these entities.[18] In this light, we hypothesize that such non-aromatic intrinsic emission can be coupled with metal-enhanced fluorescence for signal enhancement, as such strategies have already been

[a] Department of Chemistry, Indian Institute of Technology Delhi, Hauz Khas, New Delhi- 110016, India.
[b] Centrosome and Cilia Laboratory, Regional Centre for Biotechnology, NCR Biotech Science Cluster, 3rd Milestone, Faridabad-Gurugram Expressway, Faridabad, Haryana (NCR Delhi) 121001, India.
[c] Center for Advanced Materials and Devices (CAMD), BML Munjal University, Haryana, India.
[d] Department of Materials Science and Engineering, Indian Institute of Technology Delhi, Hauz Khas, New Delhi110016, India.

Electronic Supplementary Information (ESI) available: It consists of the HRTEM images, Raman spectroscopic analyses and cell viability and imaging studies.

adopted for metal-enhanced fluorescence.[11, 19, 20] The localized surface plasmon resonance of noble metal nanoparticles gives rise to intense electromagnetic intensity. It can enhance the low quantum yield and remove the requirement for higher analyte concentrations. Such technique is harnessed by several analytical tools such as surface-enhanced Raman scattering (SERS),[21-24] surface-enhanced infrared absorption, and metal-enhanced fluorescence.[25] Through the plasmon-protein conjugation, we have achieved the following targets in this work: (i) generating clusteroluminescence from protein-nanoparticle aggregates, (ii) red shifting the fluorescence to separate the target molecule's fluorescence from the autofluorescence background, often seen in the biological systems, (iii) enhancing the clusteroluminescence of the biological samples through plasmonic attachment, and (iv) applying clusteroluminescence to directly observe protein aggregation inside complex biological systems such as cells.

The fluorescence enhancement was achieved by harnessing through-space interactions from the inherently present heteroatoms within the aggregated protein-nanoparticle conjugates. The catalytic formation of nitrile on the nanoparticle surface and the restricted intramolecular motion due to the self-assembly-driven aggregation on the surface of the plasmonics contribute to the improved emission quantum yield of the biomolecules.[26] The fluorescence of the biomolecules was red-shifted due to the enhanced intra and intermolecular through-space interactions. Stark effect type of charged interactions within the aggregates also contributes to this shift. First-principle-based calculations showed the dominant interaction of nitrogen-containing groups of proteins with the nanoparticle surface. The relatively weak but evident charge accumulation on the nitrogen atom highlights the through-space intermolecular electronic coupling, which results in fluorescence emission. The charge transfer state in such a scenario with longer lifetimes has been demonstrated through transient absorbance spectroscopy studies. The overall mechanism of the clusteroluminescence is illustrated in **Figure 1.**

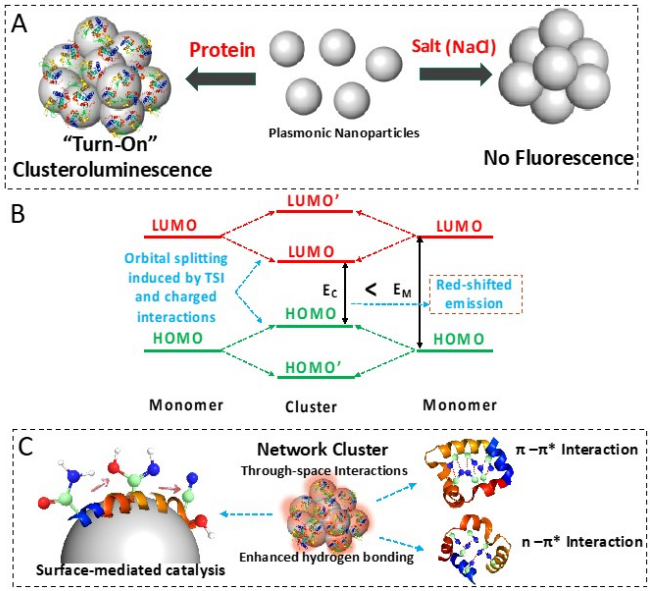

Figure 1. Schematic diagram showing the overall workflow. (A) "Turn-on" clusteroluminescence was observed when protein molecules were aggregated using colloidal AgNP. Similar fluorescence emission was absent when the AgNP were aggregated using a salt solution. (B) The electronic transitions responsible for red-shifted emission due to through-space and charged interactions. (C) The formation of species such as nitrile groups on the AgNP surface results in the through-space intermolecular electronic coupling (TSI) resulting in the clusteroluminescence phenomenon. The enhanced hydrogen bonding in the protein-AgNP aggregate and the TSI through the π –π* and n –π* Interactions also contribute to this phenomenon.

Herein, for the first time, we utilize such metal-nanoparticle-enhanced clusteroluminescence to image protein aggregates inside the cells without using any exogenous fluorophores. This phenomenon is shown by the silver nanoparticles (AgNP) which was able to induce visible or red emission from aggregation-prone Huntingtin proteins in cells in a label-free manner.[27] This study highlights the role of non-functionalized nanoparticles as they have been found to promote protein aggregation in aqueous solution and, when exposed to live cells, can do the same. Such behaviour has been observed in the case of aggregation of α-synuclein.[28] Gold nanoparticles decorated with polyglutamine-binding amphiphilic peptides have been used to target polyQ-rich mutant huntingtin proteins.[29] Interestingly, we observed a similar trend when the AgNP were incubated with HeLa cells overexpressing the Huntingtin protein. The flip from a significantly quenched fluorescence state to a highly enhanced state in the event of aggregation provides an excellent contrast ratio. It also acts as an indicator of the aggregation itself. These properties make these aggregation-induced fluorescence techniques ideal for both sensing and tracing applications.[26, 30]

2. Experimental section

2.1. Chemicals

Silver nitrate (99.99% purity), lysozyme from chicken egg white (crystalline powder, 70000 units/mg), sodium chloride (>99.0% purity), Hoechst 33342 dye, sodium citrate dihydrate (≥99.5% purity), protamine sulphate, 4-nitrothiophenol (4-NTP), thiophenol (TP), paraformaldehyde, all with 99% purity were purchased from Sigma Aldrich. Fetal bovine serum (RM9955) and trehalose (GRM-110) was purchased from Himedia, Rabbit polyclonal anti-HA antibody (1:500; BB- AB0050) sourced from Bio Bharti Life Sciences, goat anti-rabbit Alexa Fluor 647 antibody (1:2000; A21245) sourced from Invitrogen, and DMEM and penicillin-streptomycin were purchased from Gibco. Plasmid (pHM6-Q74) was received as a gift from David Rubinsztein (Addgene plasmid # 40264). Other reagents and solvents were of analytical grade and used as such without purification. MilliQ water was used for all the experiments.

2.2. Silver Nanoparticles synthesis

Lee-Meisel method was used to synthesize colloidal AgNP.[31] In 100 mL MilliQ water, 18.0 mg of silver nitrate was dissolved. 1% sodium citrate (2 mL) was added to the boiling solution. The mixture was heated with stirring for 1 h and brought to room temperature while stirring. The product obtained was a greenish-yellow colloidal fluid. Then, the obtained AgNP was characterized with several techniques. Shimadzu UV-2450 spectrometer was used to perform the UV-visible spectroscopic measurement to study the Lysozyme-AgNP interactions using a quartz cuvette having a 1 cm path length. Photoluminescence (PL) spectra were obtained for the same solution using a QuantaMaster 8450-22 Spectrofluorometer (Horiba) with excitation and emission slit widths of 3 nm and 3 nm, while the

attenuated total reflectance-fourier transform infrared (ATR-FTIR) spectra were recorded on an Agilent Cary 600 Series (Cary 660) FTIR spectrometer equipped with cryogenically cooled InSb detectors. A Tecnai TF20 electron microscope with an accelerating voltage of 200 kV was used for high-resolution transmission electron microscopy (HRTEM) imaging of the prepared AgNP and the size distribution were investigated by Dynamic light scattering (DLS) using a Zetasizer from Malvern Pananalytical.

2.3. Surface-enhanced Raman Studies

The SERS spectra were recorded using an Xplora Raman spectrometer from Horiba Jobin Yvon containing two excitation lasers of wavelength 532 nm and 785 nm and a Peltier-cooled CCD. SERS spectra were recorded with 1200 grooves per mm of holographic grating with 100 um slit width and a 10x objective. A typical spectral acquisition time was 20 s at room temperature. The Raman spectra were recorded at least three times to check the reproducibility, and the Raman at 520.7 cm^{-1} of the silicon wafer was used to calibrate the instrument.[32] The post-processing of the spectra was performed using OriginLab Pro 2020b, including background subtraction and smoothening using a 5-point FFT algorithm.

2.4. Computational methods

We have used density functional theory (DFT) based simulations as implemented in the Vienna Ab Initio Simulation Package for all the computational simulations.[33, 34] All the calculations employ the projected augmented wave method and a plane-wave basis set with a cut-off of 400 eV.[35] The generalized gradient approximation with the Perdew-Burke-Ernzerhof functional form is used for approximating the exchange and correlation interactions.[36] The geometry optimization ensures that the interatomic forces are less than 0.01 eV/Å. For these structural relaxation simulations, we employ 4×4×1 Γ-centered k-point mesh for Brillouin zone sampling. To model the noncovalent interactions, we consider the dispersion correction as prescribed by Grimme *et al*. in their DFT-D3 scheme.[37] The self-consistent field (SCF) calculations use a finer Γ-centered k-point grid of 6×6×1. The Gaussian smearing of 0.01 eV is considered for all SCF calculations. To model AgNP-molecule interactions, we construct an AgNP slab with an exposed (111) surface. The AgNP slab contains four layers of metal (64 atoms) with a 4×4 supercell in ab-plane. To introduce vacuum at nonperiodic c-direction, we increase the cell parameter by 20 Å at that direction. Such a model suppresses the spurious interaction between periodic images. The molecules are adsorbed on top of the (111) plane of AgNP to understand the AgNP layer-molecule interactions. A similar computational model has been employed by some of us recently to model the AgNP-alloy surface.[38] To model the optimized geometry and total electronic energy of isolated molecules, we keep those in the middle of the three-dimensional simulation box used for AgNP-molecule simulations. For these simulations, we use a single 1×1×1 Γ- point and retain all other parameters the same as before.

2.5. Transient absorption Spectroscopy (TAS)

Ultrafast transient absorption measurements were conducted using a commercial one-box ultrafast Ti: Sapphire (Astrella 1K-F) amplifier laser system (Coherent Inc.) pulses of 100 fs time duration, amplified pulse at 1 kHz repetition rate was obtained. The amplified pulses with 5 mJ/pulse energy were obtained after seeding with 20 fs and 70 nm bandwidth laser pulses obtained from an oscillator (Vitara-S) operating at 80 MHz repetition rate. The amplified output of central wavelength of 800 nm was divided into two parts. One part was used to produce the femtosecond probe pulse by focusing it on a CaF_2 (for UV probe: 310 – 615 nm) and 2 mm thick sapphire crystal by generating a white light continuum (400-800 nm), and the other part was used to generate a tuneable femtosecond pump pulse using an Optical Parametric Amplifier (Coherent OPeraASolo Ultrafast optical Parametric Amplifier system). After the sample, the probe beam was collimated and then focused into a fiber-coupled spectrometer with CMOS sensor (1024 pixels) and detected at a frequency of 1 kHz. The power of the pump pulse used in the experiment was controlled by a variable neutral-density filter wheel and was kept at 1 mJ/pulse. The delay between the pump and probe pulses was controlled by a motorized delay stage. The pump pulses were chopped by a synchronized chopper at 500 Hz and the absorbance change was calculated with two time-adjacent probe pulses (pump-blocked and pump-unblocked).

The samples soluble in solvent were taken in a 2 mm quartz cuvette and stirred constantly by a magnetic stirrer during the measurements. For transient measurements, 400 nm was used as the pump wavelength, and sapphire crystal was used for visible range white light as the probe. Concentrations of the freshly prepared samples were adjusted to maintain an optical density in the range of 0.02 - 0.04 in a 2 mm quartz cuvette. To check for charring or any damages in the sample during transient absorption measurements, ground state absorption spectra were taken before and after laser exposure. Surface Xplorer version 4.5 was used to analyze the transient absorption spectra.

2.6. In-cellulo AgNP labelling for cellular imaging.

HeLa cells were maintained in DMEM supplemented with 10% fetal bovine serum and 1x penicillin-streptomycin in a humidified incubator at 37 °C with 5% CO_2. For the imaging experiments, $2x10^4$ cells in the early passages (between P3-P10) were seeded 12 h prior to transfection onto 35 mm dishes containing 10 mm coverslips. Upon achieving 30% confluency, these cells were transfected with 2 µg of the plasmid (pHM6-Q74) and allowed to express the aggregation prone hemagglutinin (HA)-tagged Huntingtin (HA-HTT) for the next 48 h before harvesting. Transfected population without the AgNP were used as a control while the un-transfected cells were used as a negative control. The cells were treated with 0.5 nM AgNP suspension made in 0.25 mM trehalose 3 h prior to collection. In the end, coverslips were fixed with 2% paraformaldehyde (PFA) at room temperature for 20 min and then subsequently washed thrice with 1x PBS. These fixed cells were further labelled to visualize the HTT aggregates by immunofluorescence staining and fluorescent microscopy using a Zeiss LSM880 confocal microscope. Z-stack images (0.2 µm step size) were acquired under 63x magnification oil immersion objective lens with an N.A. of 1.4. The AgNP were excited with 488 nm laser and the emission between 550-700 nm was acquired using the HyD detectors. Similarly, the 647 and 405 nm lasers were used respectively, for HA-HTT and DNA visualization in a sequential manner. The acquired images were visualized and analyzed using ImageJ. Further, the Pearson's coefficient representing the co-localization status for the AgNP clusters and HTT aggregates was estimated across the individual HTT cluster ROIs using 30 cells (one cluster / cell) showing HTT aggregation. The mean and standard deviation (SD) were calculated for the same from three independent biological repeats and represented using the GraphPad Prism software.

2.7. Immunofluorescence assay

Briefly, cells grown on glass coverslips were fixed with 2% PFA for 20 min, permeabilized with 0.3% Tween20 for 20 min and then blocked with 5% bovine serum albumin for 1 h at room temperature. The coverslips were then incubated with a Rabbit polyclonal Anti-HA

Antibody for 1 h, followed by incubation with goat anti-rabbit Alexa Fluor 647 antibody. DNA was stained using Hoechst 33342 dye for 5 min and mounted using 70% glycerol.

2.8. Cell viability assay

HeLa cells were seeded in 35 mm dishes at a density of 0.3×10^6 and cultured overnight. At 70-80% confluency, each dish was treated with different concentrations of AgNP, i.e. 0 µL, 5 µL, 10 µL, 30 µL, 50 µL and 100 µL with equal volumes of 0.5 M trehalose solution respectively to achieve the final concentration of 0 nM, 0.08 nM, 0.16 nM, 0.5 nM, 1.6 nM, 3.2 nM respectively, and incubated for 24 h. After which cells were trypsinized and resuspended in serum-free media. One part of cell suspension i.e. 10 µL was mixed with one part of 0.4% trypan blue and allowed to incubate ~1 min at room temperature and the cells were counted, unstained (viable) and stained (nonviable) separately in the haemocytometer.

3. Results and discussion

The main aim of this study was to comprehensively probe the mechanism behind the intensified, red-shifted fluorescence observed in protein-nanoparticle conjugates. This distinctive optical trait was targeted for its potential in imaging of a neurodegenerative disease. The underlying mechanism responsible for the emergence of the "turn-on" far-red fluorescence within non-fluorescent protein-nanoparticle aggregates was investigated by combining spectroscopic techniques and quantum theoretical calculations.

3.1. Protein-nanoparticle interactions and the characterization of the aggregates

The size of AgNP employed in the experiments was 60 nm, with the localized surface plasmon resonance (LSPR) peak at 410 nm. The size of the nanoparticles was confirmed by TEM (**Figure S1**). For an in-depth exploration of surface interactions of proteins at the molecular level, lysozyme was used as an appropriate model protein due to its well-established characterization and several biologically significant applications. Of significance, lysozyme, a globular protein, has demonstrated interactions with nanomaterials that lead to amyloid-type aggregates.[39] The LSPR was obtained through UV-visible spectroscopy both in the presence and absence of the protein. The positive charge on the lysozyme surface at physiological pH is due to its isoelectric point around 11, which facilitates attachment with the negatively charged AgNP. It has been shown previously that a dynamic equilibrium exists between the adsorbed protein

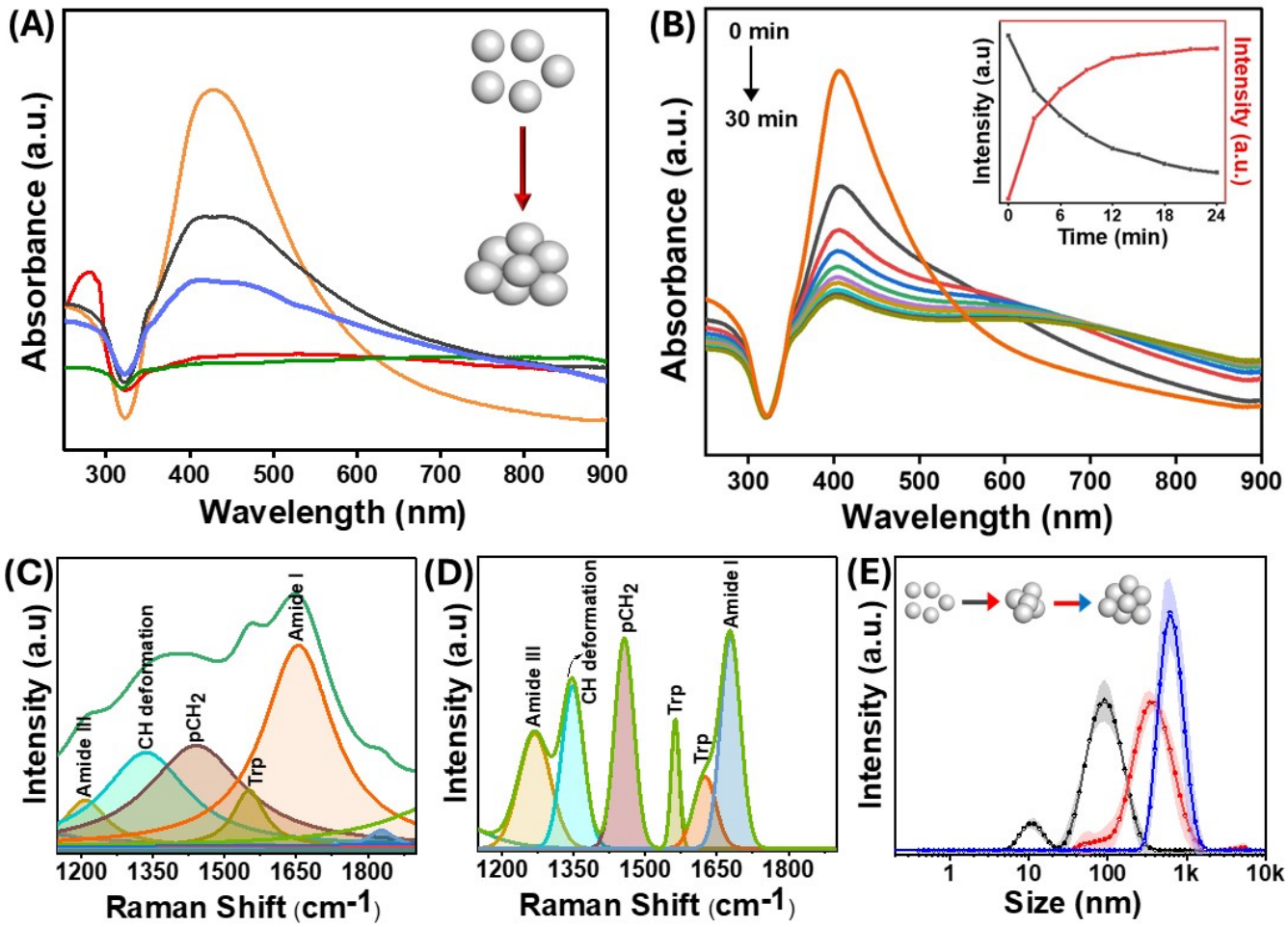

Figure 2.(A) UV-visible spectra of lysozyme-AgNP complex with different concentrations of protein [10^{-3} M (red), 10^{-5} M (green), 10^{-7} M (purple), 10^{-9} M (black), AgNP (orange)] and incubated for 30 min, **(B)** Time dependent UV-visible spectra from 0 to 30 min. The inset shows the variation of dipolar plasmonic peak intensity (Black) and longitudinal tail intensity (Red) with time. Deconvoluted SERS spectra of **(C)** the lysozyme-AgNP complex and **(D)** Pure lysozyme showing the change in secondary structure of proteins. **(E)** Dynamic light scattering spectra AgNP (black), salt aggregated AgNP (red), Protein aggregated(blue) showing the different size distribution of the aggregates, while the shaded part of line corresponds to error bar. A protein concentration of 10^{-5} M was used in the lysozyme-AgNP conjugates used in **(B-E)**.

molecules on the nanoparticle surface, and the point of interaction is not random but through specific domains on the protein.[40] When lysozyme is added to the AgNP, a slight change in the location of the LSPR band was observed, which was attributed to the change in the refractive index surrounding the nanoparticle (**Figure 2(A and B)**). Interestingly, when the nanoparticles were incubated with different protein concentrations, a drastic change in the longitudinal surface plasmon resonance peak in the UV-visible spectrum was observed (**Figure 2(A)**). The transverse plasmon band of AgNP was significantly diminished, accompanied by increased longitudinal (tail) band intensity. Such observation is typical of the formation of protein-nanoparticle aggregates as reported by Halas et al.[41] Since the protein molecules undergo partial denaturation on the surface of the nanoparticles, the favourably interacting domains come together and form amyloid-type aggregates, thus pulling the nanoparticles together. This results in the loss of the dipolar plasmon peak as the particles are no longer spherical and aggregated together to form differently-sized nanoparticle clusters. This gives rise to the increasing intensity of multipolar LSPR modes at a higher wavelength (around 800 nm), and the heterogeneity of the system makes the peak much broader.[42] The change in the LSPR profile indicates that the maximum aggregation occurs at the concentration of 10^{-5} M of protein incubated with 0.5 nM of the AgNP. Furthermore, the change in the protein structure due to surface-induced aggregation was observed from the changes in the intensity of the characteristic peaks of Lysozyme in the UV-visible spectrum around (260 nm - 280 nm) **(Figure 2(A)).** These peaks emerge due to the lateral chains of aromatic residues like tyrosine, tryptophan, phenylalanine, and cysteine. The changes in protein structure could also be observed through the deconvolution of the amide I band of the SERS spectra of the protein-nanoparticle conjugates (**Figure 2(C) & 2(D)**). The protein exhibits alterations in its conformational state, specifically in the proportion of its helical secondary structure following the aggregation process. Consequently, a reduction of 6% in helical conformation was observed as compared to the native protein.

In addition to the appearance of multipolar surface plasmon modes, the time-dependent UV-visible spectrum in **Figure 2(B) and Figure S2** shows a blue shift in the transverse surface plasmon mode of AgNP with the increase in the incubation time. This blue shift in the absorption spectrum of AgNP can be due to events such as leaching or charge transfer at the protein-nanoparticle interface.[43] The addition of Lysozyme resulted in a slight increase in the hydrodynamic diameter of bare

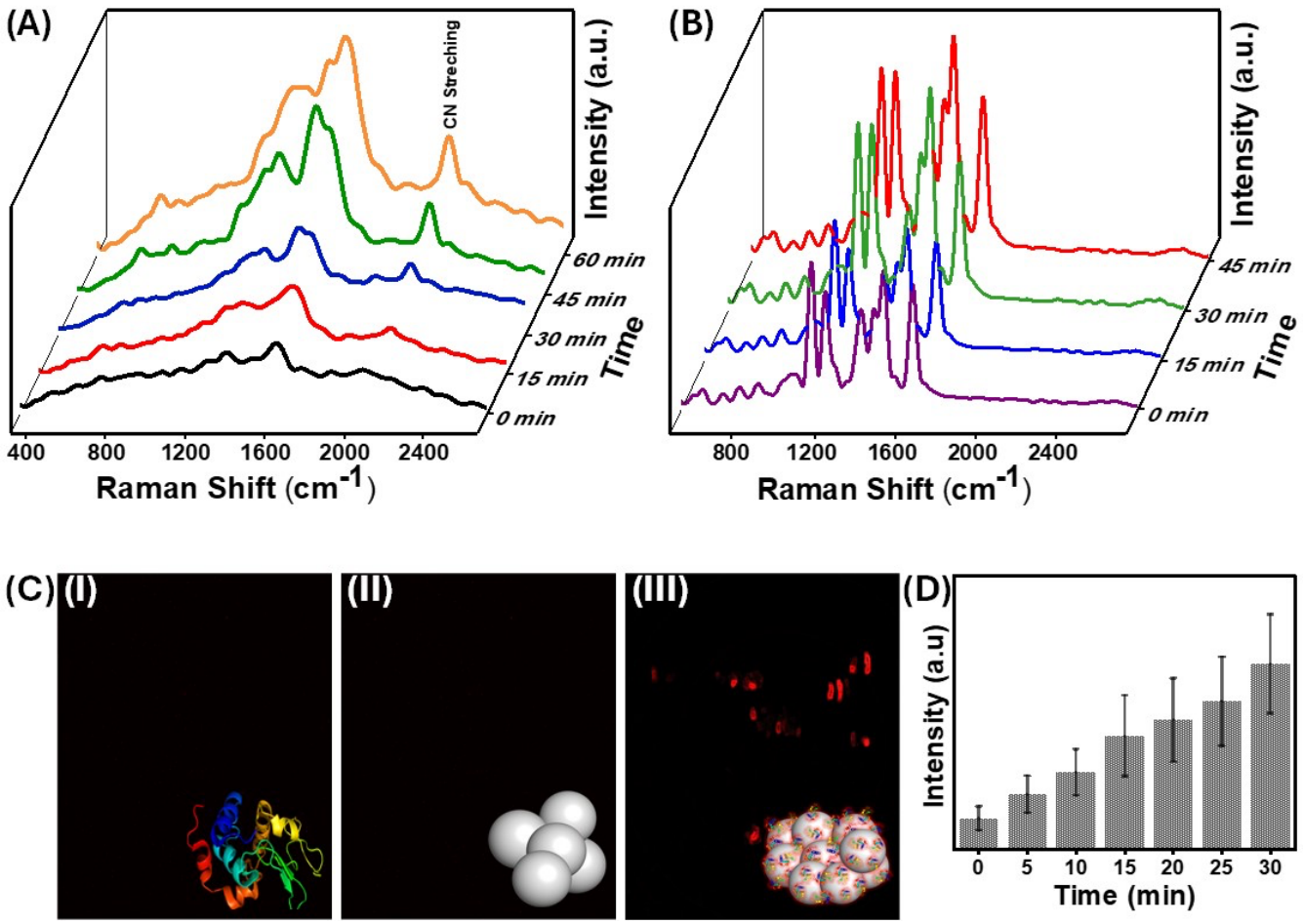

Figure 3. SERS spectra **(A)** lysozyme aggregated AgNP at different time points, and **(B)** salt aggregated AgNP with 4-NTP at different timepoints. The SERS spectra were collected using a 532 nm laser source. **(C)** Confocal fluorescence images of **(I)** AgNPs, **(II)** lysozyme, and **(III)** AgNP incubated with lysozyme (10^{-5} M) obtained with a laser excitation source of 543 nm, **(D)** Time dependent fluorescence intensity variation calculated from the confocal fluorescence images.

nanoparticles, which was directly observed by the DLS technique. The formation of large aggregates of AgNP as a function of time was evident from the evolving hydrodynamic radius of nanoparticles incubated with lysozyme (**Figure 2(E)**).

Since charge-based interactions are critical for aggregate formation, we have also investigated the effect of ionic species such as salts. **Figure 2(E)** compares the sizes of salt and protein-induced nanoparticle aggregates. The size distribution plots from the DLS data revealed that the lysozyme-catalyzed aggregation produced tightly packed and well-ordered aggregates. The analysis of the full-width at half maximum of these peaks showed that the polydispersity of the salt-aggregated AgNP was more pronounced than those formed using lysozyme. These observations indicate the possible existence of an additional interaction mechanism between the protein and the nanoparticles, specifically at the interface, which is discussed in the subsequent sections.

3.2. The emergence of far-red fluorescence from the protein-nanoparticle aggregates

SERS, a predominantly surface-sensitive technique, was used to explore the precise mechanism of the interactions between proteins and nanoparticles. SERS has been recently used to probe minute structural changes in the binding of proteins to the surface of nanoparticles.[44-46] The vibrational features of aromatic amino acids Phe, Tyr, and Trp, as well as amide and protein secondary structural characteristics, dominate the SERS spectrum of lysozyme, which is consistent with previous research.[47, 48] It is worth noting that the position and amplitude of the protein's modes are influenced by its orientation to the nanoparticles' surface, which is determined by surface selection criteria.[49] Because the electromagnetic field augmentation decays with the third power of the circumferential distance from the surface, vibrational modes near the surface are enhanced more than those further away.[50] Interestingly, as the aggregation of the protein-nanoparticle conjugate increases with time, the fluorescence background seen from SERS also increases, indicating the emergence of a “turn-on” fluorescence in the system (**Figures 3(A) and S3)**.

The evolution of protein-induced nanoparticle aggregation with time and the corresponding fluorescence emission were monitored using confocal fluorescence microscopy **[Figure 3]**. An increase in the fluorescence intensity with incubation time was observed, as the aggregation is a time-dependent phenomenon.[41] The extent of aggregation could be directly correlated to the increase in the fluorescence emission intensity. Confocal microscopy also showed this red-shifted fluorescence, aligning with the substantial fluorescence background noted earlier in the SERS of the same samples. In **Figure 3(C)-(i)**, it could be seen that the confocal fluorescence microscopy image of the pure and fresh lysozyme solution obtained with 543 nm laser excitation had no fluorescence emission. Similarly, no red fluorescence was observed in the case of bare AgNP **[Figure 3(C)-(ii)]**. However, when the nanoparticles were aggregated using Lysozyme, they exhibited a strong red fluorescence [**Figure 3(C)-(iii)]**. The red emission was observed in the range of 645-680 nm. Contrasting results were obtained when the same AgNP were aggregated with sodium chloride, and no fluorescence emission could be observed.

Interestingly, small molecules such as 4-NTP also displayed fluorescence emission from the Raman and the fluorescence data. However, the confocal fluorescence image of the aggregated nanoparticles in the presence of TP, where nitrogen and oxygen atoms are absent, showed no fluorescence emission **(Figure S4),** which essentially highlights the role of functional groups containing these atoms in fluorescence emission in the red region. This unique emission has been observed previously in a few reports and also in the case of clusteroluminescence.[51, 52] Even non-conjugated systems possessing lone pair-containing atoms also have enhanced red-shifted emissions.[53, 54] Therefore, biomolecules containing a high percentage of nitrogen-containing functional groups show

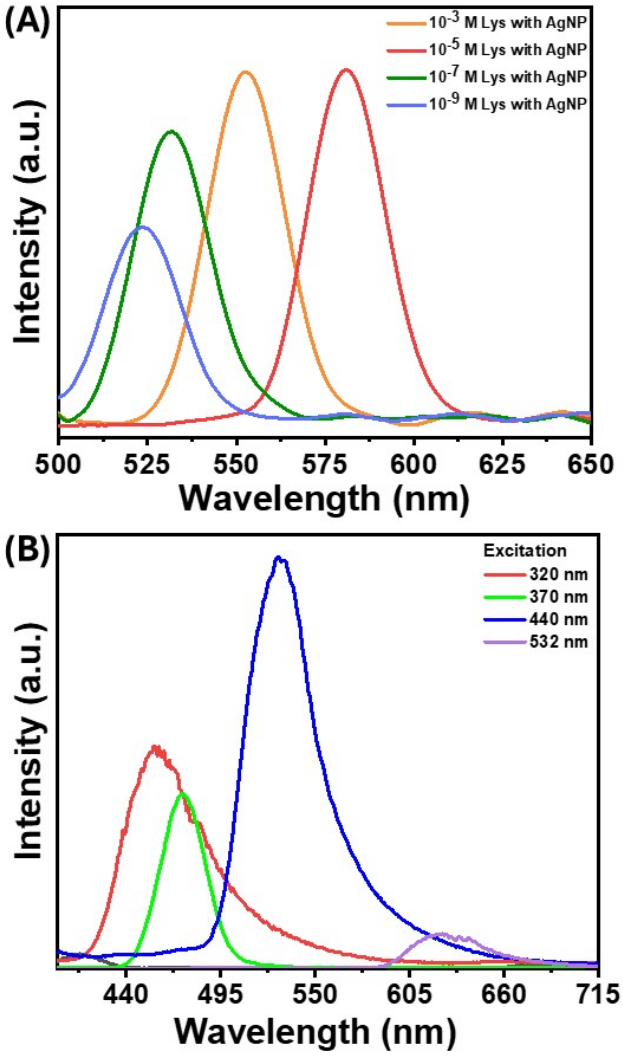

Figure 4. (A) PL spectra of AgNP-lysozyme complex with different concentrations of lysozyme. **(B)** Laser excitation-dependent PL spectra of AgNP aggregates in presence of Lysozyme.

clusteroluminescence and cluster-dependent biological activities.[18, 55] In the subsequent sections, we investigated this unique emission through various spectroscopic techniques.

3.3. Spectroscopic analysis of the origin of the red emission from the nanoparticle-protein conjugate.

Absorbance and emission spectroscopy provided significant insights into the photo-physics of the system. Protein-nanoparticle aggregates of different sizes were created using different nanoparticle-to-protein ratios, and their average hydrodynamic radius was obtained by DLS. The emission spectra of these different aggregates were found to be red-shifted with the increase in sizes **(Figure 4(A))**. Unlike conventional fluorescence, the emission wavelengths varied when the same aggregate was excited by different excitation wavelengths **(Figure 4(B))**. This excitation-dependent luminescence is a unique feature of clusteroluminescence. According to Kasha's rule, luminescence happens from the lowest excited state, and the emission wavelength is constant for a particular molecule with a definite structure, due to which the change in excitation will only result in the change in the emission intensity but not the emission wavelength.[56] However, in the case of clusteroluminescence, the electron delocalization differs in the clustered state, resulting from the different energy gaps of the emitters. These results confirm the emergence of clusteroluminescence from the protein-nanoparticle aggregates.

Since the fluorescence in proteins emerges from aromatic amino acids such as Trp, Tyr, His, and Phe, the initial hypothesis was that proteins bereft of these amino acids would not show such red-shifted fluorescence. However, a small positively-charged protein molecule, protamine sulphate, which lacks amino acids, also produced considerable fluorescence background on aggregation (**Figure S5(A)**). The SERS background fluorescence from protamine was higher than 4-NTP (**Figure 3(B)**) and TP (**Figure S5(B)**), where the nanoparticle-molecule conjugates were aggregated using salt solutions. These observations point toward specific surface chemistries on nanoparticles, giving rise to this "turn-on" fluorescence. The interaction of the protein with the nanoparticles was further studied through the ATR–FTIR, which provided information on molecular-scale site-specific interactions. The ATR spectrum from the nanoparticle-protein conjugate showed new peaks in the 2200–2400 cm^{-1} range. **Figure 5(A)** shows the infrared spectra of Lysozyme incubated with AgNP at different durations. The newly emergent peak at 2330 cm^{-1} can be assigned to the nitrile (CN) triple bond stretching mode, as reported earlier.[57] As the concentration of the nitrile group increases with the incubation time, the intensity of this peak increases. Therefore, it can be concluded that some of the amine or amide bonds were successfully converted to the nitrile group. The nitrile group absorbs at 2250-2270 cm^{-1} and is well-separated from naturally occurring vibrational modes in proteins. The local environment might vary dramatically within a protein (the bond in question might be in proximity or buried in the protein's hydrophobic core), which causes the absorption

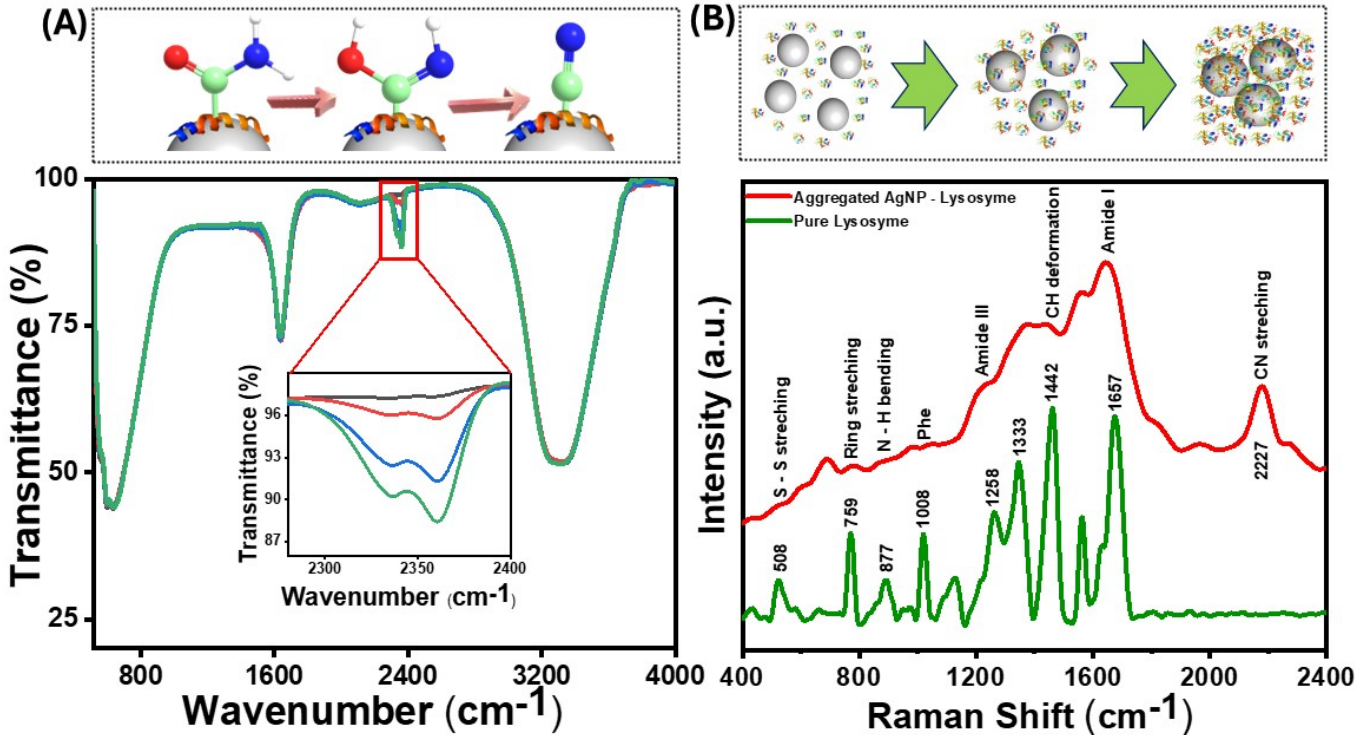

Figure 5. (A) (Top) Pictorial representation of conversion of amide to nitrile. The carbon, nitrogen and oxygen atoms are shown in light green, blue and red respectively. The ribbon representation depicts the adsorption of the protein and the AgNP-mediated catalysis happening on the AgNP surface (shown as grey sphere). (Bottom) ATR-FTIR spectra of the lysozyme-AgNP complex containing 10^{-3} M (green), 10^{-5} M (blue), 10^{-7} M (red), 10^{-9} M (black) lysozyme concentrations (inset shows the zoomed view from 2250-2400 cm^{-1}). **(B)** (Top) Schematic of nanoparticle-induced formation of protein aggregates. (Bottom) Raman spectra of lysozyme (green) and lysozyme-AgNP complex (red).

peak of the nitrile group to shift to around 2330 cm^{-1}. The amine or amide group can be converted to the nitrile group through various mechanisms, such as the silver-catalyzed dehydration of the amide bond or the silver-catalyzed oxidation to the nitrile group[58]. As the aggregation increases, the reactive sites captured between the aggregates are locked at a specific position, making the conversion more probable. So, the silver atom catalyzes the formation of the nitrile group by acting as the electron acceptor from the nitrogen atom in the peptide chain, as confirmed by the charge transfer quantum calculation between the Ag surface and the binding moieties. As reported in earlier studies, Nitrile group clusters have been strongly linked to the hyperbranched-enhanced-emission effect due to the through-space conjugation.[59] These moieties or sub-fluorophores, such as -NH-, C=O, and nitrile, are generally composed of electron-rich heteroatoms and exhibit unusual fluorescence due to the formation of a pendent group cluster. This clusterization-mediated restricted movement of the nitrile groups triggers the emission caused by non-radiative relaxation and electron delocalization by through-space conjugation.[38] We envisage that the oxygen-rich moieties in the protein molecules, specifically the formation of silver-catalyzed nitrile group on the surface of the AgNP, give rise to the clusteroluminescence in the nanoparticle aggregates.

The emergence of a nitrile group can also be seen from the SERS spectra of lysozyme **(Figure 5(B))** and protamine sulphate **(Figure S5(A))**, along with a significant fluorescence background when excited with a 532 nm laser source. The SERS band around 1442 cm^{-1} is due to the methylene group, and the band corresponding to 877 cm^{-1} is assigned to Trp. This band belongs explicitly to the N-H site of the indole ring on aggregation inside the Trp moiety and is sensitive to environmental change.[50] The peak at 233 cm^{-1} is assigned to the Ag-N bond, which explains the binding site to AgNP. The nitrile peak at 2227 cm^{-1} increased with the nanoparticle incubation time and the consequent increase in aggregation. However, this peak was absent in the SERS spectra of TP, further highlighting the surface-catalyzed conversion of the nitrogen-containing functional groups to the nitrile group and its role in inducing red emission due to the clusteroluminescence.[60]

The significant red-shift of the emission can be attributed to the interaction of the dipole moment of the luminogens with the electrostatic charges within the protein-nanoparticle aggregate.[61] This interaction can be compared to the Stark effect, where the dipole moment is renormalized. The altered dipole can change the energy gap between the highest occupied molecular orbitals and the lowest unoccupied molecular orbitals, causing the observed red shift during emission.[20] The red emission can also be attributed to the coexistence of intrachain and interchain through-space interactions of the luminogens in the aggregated protein molecules. The aggregated state also promotes abundant intramolecular and intermolecular hydrogen-bond interactions, which imparts stability to the through-space n···n (N···O) and n···π (N···C=O) type of interactions. Electrons from peptides can be delocalized through intramolecular or intermolecular hydrogen bond formation and have been previously found to have electronic transitions at longer wavelength regions, resulting in the red shift in the emission spectrum.[62]

3.4. Protein-nanoparticle charge transfer probed through quantum calculations and ultrafast spectroscopy.

To understand the atomistic details of interactions between the AgNP surface and different building units of protein, we performed thorough first-principle-based computational investigations. We initially optimized the ground state of the adsorbed molecules on the AgNP surface at 0 K. The (111) surface of AgNP has been considered for exploring molecular interactions with these metal nanoparticles. **Figure 6(A) and Table 1** include the optimized geometries and detailed structural parameters.

Table 1 I The binding energy, charge transfer, and surface-anchoring atom distances for various molecular moieties on AgNP (111) surface.

Molecules	Binding Energy (meV/atom)	Charge transfer (e^-)	Ag-N/O distance (Å)
$NCNHCH_3$	-28.3	+0.05 (molecule to AgNP)	2.29
$OHCOCH_3$	-27.0	+0.05 (AgNP to molecule)	2.86
$NHCHCH_3$	-31.1	+0.05 (molecule to AgNP)	2.57

The molecular moieties in the protein are expected to interact with the AgNP (111) surface while forming aggregates. The anchoring atoms (O and N) of the molecules remain placed on

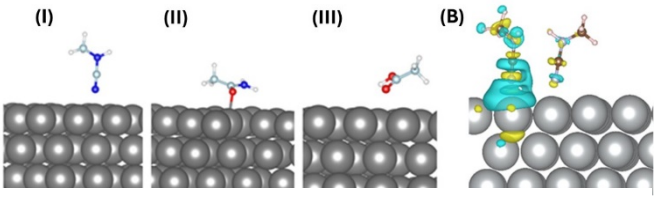

Figure 6. (A) The optimized structures of molecular moieties on the AgNP (111) surface. The surface with **(i)** $NCNHCH_3$, **(ii)** $OC(NH_2)CH_3$, and **(iii)** $OHC(O)CH_3$ are presented. The non-covalent interactions between Ag atoms and anchoring atoms (C/N) give rise to physiosorbed molecules of the surface. Key: AgNP (gray), C (cyan), N (blue), O (red), H (white). **(B)** The charge transfer between single CH_3NCN and CH_3NCN-AgNP (111) surface. The yellow and blue iso-surfaces indicate charge depletion and accumulation, respectively. The charge transfer plot depicts intermolecular as well as molecule-AgNP (111) surface electronic coupling.

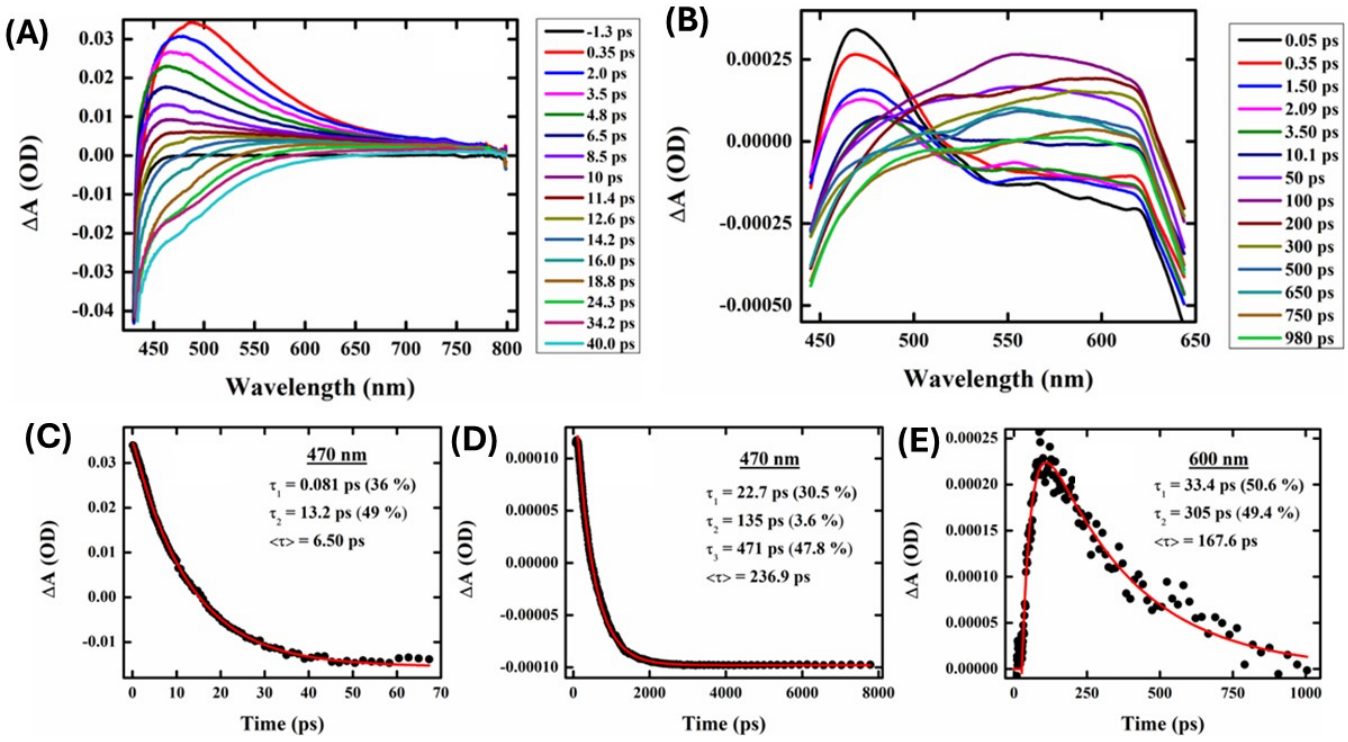

Figure 7. Transient Absorption Spectra of **(A)** AgNP and **(B)** AgNP with protein and Principal wavelength decay kinetics of **(C)** AgNP at 470 nm and AgNP with protein probing at **(D)** 470 nm and **(E)** 600 nm.

top of surface AgNP. The non-aromatic molecular moieties with different anchoring groups exhibit physisorption and shorter AgNP-X (X= anchoring atom) distances (2.29 Å – 2.86 Å), as shown in **Table 1**. The calculated binding energies for different protein moieties narrowly range from -27 to -31 meV/atom, indicating weak but stable nanoparticle–protein interactions at ambient conditions.

The intermolecular interactions between adjacent fluorescent CH_3NCN molecules on the AgNP (111) surface were studied computationally. Note that we are only considering nitrogen-containing fluorescent moiety for all further studies. The modelled supercell of the AgNP surface contains two CH_3NCN molecules that are spatially close to each other (**Figure 6(B)**). The binding energy calculations in the presence and absence of the AgNP (111) surface depict that these molecules remain stacked only on the metallic surface. The positive binding energy of 0.11 eV between pairs of molecules in the gas phase indicates that AgNP plays a crucial role in aggregating these molecules by initiating intermolecular electronic coupling. The aggregation of molecules on the surface of AgNP (111), further suggests their limited thermal motion, which can enhance the emission properties of the overall system by suppressing non-radiative recombination processes. As tabulated in **Table 1**, the Bader charge calculation depicts the direction of charge transfer between the binding entities that closely depend on anchoring groups' chemical nature. The interacting nitrogen atoms donate electrons to the AgNP surface, whereas moieties with oxygen as the binding site accept electrons from the metal surface.

The charge density difference was also studied to understand the electron transfer between protein moieties and AgNP surfaces. The plotted charge density difference reveals that the non-covalent interaction between AgNP (111) surface and nitrogen of CH_3NCN is the dominant kind of electronic coupling present in these systems, as shown in **Figure 6(B)**. Moreover, relatively weak but evident charge accumulation on the nitrogen atom of the NCN group away from the AgNP surface in one of the molecules depicts the through-space intermolecular electronic coupling.[15] The lone pair of anchoring nitrogen of CH_3NCN donates the electron cloud to the AgNP surface atoms, depicting metal surface–molecule electronic coupling. Thus, the overall charge transfer and electronic coupling between protein and AgNP can be tuned by modifying anchoring group chemistry.

The charge transfer processes that AgNP experience when interacting with proteins were probed through TAS. AgNP **(Figure 7(A))** exhibited prominent excited state absorption with a maximum at about 470 nm, showing no probe dependency on the decay kinetics. A faster interband transition to the ground state occurred within ~6.5 ps of the same probe pulse at 470 nm in the presence of AgNP **(Figure 7(B)).** On the other hand, AgNP exhibit intriguing probe-dependent dynamics in the presence of protein (~10 μM) **(Figure 7(C))**, which depicts the formation of a photoproduct state (525-650 nm) at the compensation of AgNP decay followed by its progressive ground state transition. Proteins are found to delay the electron-hole recombination time in AgNP up to ~237 ps (at 470 nm), which is the probable signature of charge transfer from the

nanoparticle to the protein **(Figure 7(D))**. The growth component of 33 ps further confirms the formation of a new photoproduct with an absorption around 600 nm, which decays down within 305 ps **(Figure 7(E))**. Therefore, these ultrafast measurements further confirm the electron transfer between the nitrogen and oxygen atoms of the proteins with the AgNP surface.

3.5. Utilizing clusteroluminescence for imaging huntingtin protein aggregates in cells.

Clusteroluminescence-based cellular imaging of Huntingtin protein aggregates overexpressed in HeLa cells was performed after AgNP labelling. Upon overexpressing the HA tagged Human Huntingtin (HA-HTT) partial exon (1- Q74) in HeLa cells for 48 h, the protein aggregates were labelled in the presence or absence of AgNP (0.5 nM) suspension for the final 3 h prior harvesting **(Figure 8A)**. Untransfected cells were used as a negative control, and similarly, the overexpressing population without the AgNP labelling was used as an additional negative control to trace the protein aggregates. Interestingly, our observations revealed that exclusively the cells marked with AgNP exhibited positive for clusteroluminescence. when excited at 488 nm wavelength. Moreover, the cells expressing the aggregation-prone species, which were colocalized with the HTT clusters, which were labeled using an anti-HA tag antibody detected with Alexa Fluor 647 conjugated secondary antibody excited at 647 nm **(Figure 8B)**. Whereas the untransfected population failed to form these protein aggregates, no clusteroluminescence was observed in these negative control cells as expected, and no signal was seen in either of the control cells. The co-localization was also confirmed through the visualization of the aggregates along with nucleus through Hoechst 33342 dye staining. The z-stacking image of the HTT aggregates with AgNPs showing clusteroluminescence clearly shows their localization within the cells (as shown in **Movie M1 and Movie M2**). Thus, the surface of plasmonic AgNP enables a complex interplay of various forces between the nanoparticle and proteins, and the chemical reactions catalyzed by the constituent materials, as shown in the earlier sections. This study is also consistent with earlier reports of metallic gold nanoparticles, which have been found to interact with proteins and interfere with amyloid formation. Proteins have a high affinity to adsorb to nanosurfaces.[63] The nanoparticles also attach oligomeric and aggregated species, particularly soft and flexible proteins and aggregates, which have larger residence times on the nanoparticle surface and dictates the stability or toxicity of the system. Trypan blue viability assays demonstrated that concentrations exceeding 0.5 nM exhibited cytotoxicity, as depicted in **Figure S6(B)**. Furthermore, extending the duration of AgNP labelling up to 24 h did not yield any significant increase in clusteroluminescent signal, as evidenced by **Figures S6(A) & S6(C)**. The observed mean Pearson's coefficient (R= 0.5802) between AgNP and HA-HTT signals in green and magenta underscores a robust positive correlation between clusteroluminescence emanating from AgNP and its specific binding to HTT protein aggregate clusters within cells. The direct observation of AgNP aggregation with protein molecules again corroborates the specificity of the AgNP to exhibit "turn-on" clusteroluminescence when they are

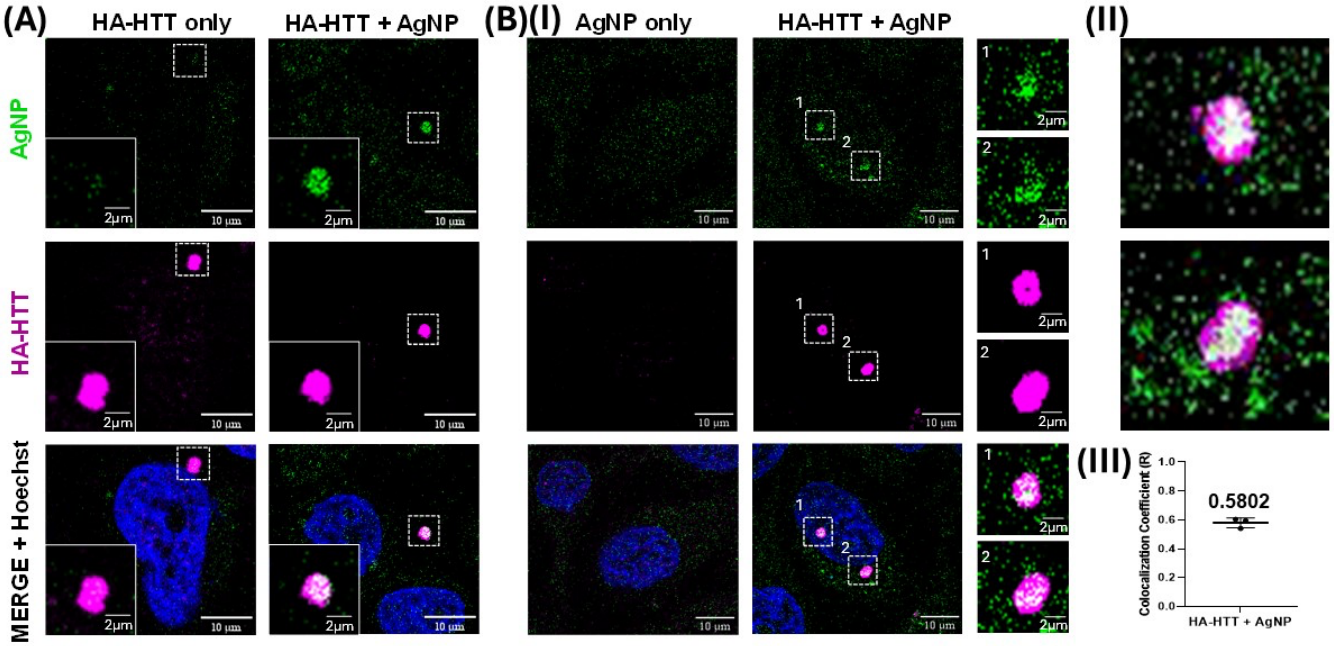

Figure 8. ***Clusteroluminescence labelling of Huntingtin protein aggregate using AgNP in HeLa cells:*** **(A) Cells expressing the aggregation prone HA tagged Huntington protein (HA-HTT) were allowed to form the aggregated and the luminescence (green) was traced in the 488 nm excitation range with and without the AgNP. (B) (I) Similarly, HeLa cells with or without the expression of HA-HTT were assessed for luminescence in the presence of AgNP. Snapshots from the 3D projection videos of the insets are shown in the XZ rotational axis in panel (II), while the Pearson's coefficient (R) for colocalising green and magenta signals are quantified with 30 individual images across three independent biological replicates and represented as a dot plot indicating the mean 0.5802 with a p value of 0.0012 is shown in panel (III). Error bar represents SD. Magenta represents anti-HA staining while green represents the clusteroluminescent signal from AgNP. DNA is visualised with Hoechst 33342 dye shown in cyan.**

strictly in a bound form with the protein aggregates, which is the Huntingtin protein in this case. The plasmonic nanoparticles and the protein-nanoparticle aggregate ensure 1) higher emission intensity from the clusteroluminogens on the nanoparticle surface and 2) red-shifting of the fluorescence to differentiate from autofluorescence and increased detection selectivity. Since the emission depends on the excitation wavelength, the interfering optical windows can be selectively avoided. We anticipate that the "turn-on" clusteroluminescence would provide a simple, robust, and functional method for molecular imaging and increase the accuracy of diagnosing such debilitating diseases.

4. Conclusions

An alternative method of label-free imaging of protein aggregates in cells is demonstrated using clusteroluminescence. Plasmonic AgNP undergo aggregation with protein molecules, leading to unconventional "turn-on" fluorescence in an aggregated state that is significantly red-shifted. This clusteroluminescence results from the interaction of the electron-rich nitrogen heteroatoms at the nanoparticle interface, specifically the plasmon-catalyzed nitrile groups, which contributes to the through-space intermolecular electron coupling, leading to fluorescence emission. The red-shift results from the hydrogen-bonded solid network of the aggregated protein molecules, which has higher electron delocalization and Stark effect type of phenomenon where the charged aggregates enable the renormalization of dipoles and change of the HOMO-LUMO energy gap. This combined effect of plasmonic enhancement and the clusteroluminescence in the protein-nanoparticle aggregates was harnessed to visualize intracellular accumulations of huntingtin proteins. Such an unconventional, red-shifted fluorescence can potentially facilitate fluorescence imaging of biological systems with minimum interference from the physiological environment.

Author Contributions

Ashish Kumar Dhillon: Conceptualization, investigation and analysis; writing – original draft; writing – review and editing. **Pranay Eknath Dudhe**: cellular investigation and analysis; writing – review and editing. **Shubhangi Majumdar:** Transient absorbance spectroscopy investigation and analysis; writing – original draft. **Sanmitra Barman:** writing – review and editing; **Dibyajyoti Ghosh:** Conceptualization; investigation, first-principle calculations and analysis; writing – review and editing. **Karthigeyan Dhanasekaran**: Conceptualization; funding acquisition; cellular investigation and analysis; writing – review and editing. **Soumik Siddhanta**: Conceptualization; funding acquisition; investigation; project administration; supervision; writing – original draft; writing – review and editing.

Conflicts of interest

There are no conflicts to declare.

Acknowledgements

This work was supported by the IIT Delhi SEED grant (IITD/Plg/Budget/2020-2021/204758), DST SERB (SRG/2020/000440), and CSIR Research grant (01(3042)/21/EMR-II). AKD thanks UGC, Government of India, for the student fellowship. S.M. thanks MHRD (Govt. of India) for the Prime Minister's Research Fellowship (PMRF ID: 1401240). AKD acknowledge the central research facility, IIT Delhi, for the usage of TEM, PL, and departmental instrument facility for characterizations. SM and SS acknowledges the Department of Science and Technology, DST-FIST (SR/FST/CS-II027/2014), New Delhi, India, for providing funds for the ultrafast TA facility. DG acknowledges the IIT Delhi SEED Grant (PLN12/04MS), the Science and Engineering Research Board (SERB), Department of Science and Technology (DST), India for Start-up Research Grant SRG/2022/00l234 and the IIT Delhi HPC facility for computational resources. This work was performed, in part, at the Center for Integrated Nanotechnologies, an Office of Science User Facility operated for the U.S. Department of Energy (DOE) Office of Science by Los Alamos National Laboratory (Contract 89233218CNA000001) and Sandia National Laboratories (Contract DE-NA-0003525). KD acknowledges RCB, Faridabad core funding, IIT-D & RCB collaborative grant and central instrumentation facilities for supporting this work. KD being a Ramalingaswami fellow (BT/RLF/Re-entry/47/2020) his research activities are partly funded by the Department of Biotechnology (DBT), Ministry of Science and Technology, India and partly by Start-up Research Grant (SRG/2021/001466), from the Science and Engineering Research Board (SERB), Department of Science and Technology (DST), India.

References

1. J. D. Ciubuc, K. E. Bennet, C. Qiu, M. Alonzo, W. G. Durrer and F. S. Manciu, *Biosensors*, 2017, **7**, 43.
2. S. Ashrafpour, T. T. Moghadam and B. Ranjbar, *International Journal of Chemical and Molecular Engineering*, 2014, **8**, 985-988.
3. W. R. Silva, C. T. Graefe and R. R. Frontiera, *Acs Photonics*, 2016, **3**, 79-86.
4. A. Vertegel, R. Siegel and J. Dordick, *Langmuir*, 2004, **20**, 6800-6807.
5. X. Wu and G. Narsimhan, *Biochimica Et Biophysica Acta-Proteins and Proteomics*, 2008, **1784**, 1694-1701.
6. G. Vecchio, A. Galeone, V. Brunetti, G. Maiorano, L. Rizzello, S. Sabella, R. Cingolani and P. Pompa, *Nanomedicine-Nanotechnology Biology and Medicine*, 2012, **8**, 1-7.
7. J. Karlo, A. K. Dhillon, S. Siddhanta and S. P. Singh, *Journal of Biophotonics*, 2023, e202300341-e202300341.
8. A. J. Schain, R. A. Hill and J. Grutzendler, *Nature medicine*, 2014, **20**, 443-449.
9. A. K. Dhillon, A. Sharma, V. Yadav, R. Singh, T. Ahuja, S. Barman and S. Siddhanta, *Wiley Interdisciplinary Reviews: Nanomedicine and Nanobiotechnology*, 2023, e1917.
10. J. Karlo, A. K. Dhillon, S. Siddhanta and S. P. Singh, *Journal of Biophotonics*, 2023, **16**, e202200341.
11. H. Szmacinski, K. Ray and J. R. Lakowicz, *Analytical biochemistry*, 2009, **385**, 358-364.
12. T. Imoto, L. S. Forster, J. A. Rupley and F. Tanaka, *Proceedings of the National Academy of Sciences*, 1972, **69**, 1151-1155.

13. B. He, J. Zhang, J. Zhang, H. Zhang, X. Wu, X. Chen, K. Kei, A. Qin, H. Sung, J. Lam and B. Tang, *Advanced Science*, 2021, **8**.
14. A. D. Stephens, M. N. Qaisrani, M. T. Ruggiero, G. Díaz Mirón, U. N. Morzan, M. C. González Lebrero, S. T. E. Jones, E. Poli, A. D. Bond and P. J. Woodhams, *Proceedings of the National Academy of Sciences*, 2021, **118**, e2020389118.
15. H. Zhang and B. Z. Tang, *Jacs Au*, 2021, **1**, 1805-1814.
16. Q. Wang, X. Dou, X. Chen, Z. Zhao, S. Wang, Y. Wang, K. Sui, Y. Tan, Y. Gong, Y. Zhang and W. Yuan, *Angewandte Chemie-International Edition*, 2019, **58**, 12667-12673.
17. M. Mittal, S. Gautam, P. K. Chowdhury, S. Deep and S. Sapra, *Zeitschrift für Physikalische Chemie*, 2019, **233**, 41-54.
18. H. Zhang, Z. Zhao, P. McGonigal, R. Ye, S. Liu, J. Lam, R. Kwok, W. Yuan, J. Xie, A. Rogach and B. Tang, *Materials Today*, 2020, **32**, 275-292.
19. B. Lochocki, B. D. C. Boon, S. R. Verheul, L. Zada, J. J. M. Hoozemans, F. Ariese and J. F. de Boer, *Communications biology*, 2021, **4**, 474.
20. S. Sarkar, B. Kanchibotla, J. D. Nelson, J. D. Edwards, J. Anderson, G. C. Tepper and S. Bandyopadhyay, *Nano letters*, 2014, **14**, 5973-5978.
21. N. Abu Hatab, J. Oran and M. Sepaniak, *Acs Nano*, 2008, **2**, 377-385.
22. A. Campion and P. Kambhampati, *Chemical Society Reviews*, 1998, **27**, 241-250.
23. K. Ikeda, S. Suzuki and K. Uosaki, *Journal of the American Chemical Society*, 2013, **135**, 17387-17392.
24. R. Livingstone, X. Zhou, M. Tamargo, J. Lombardi, L. Quagliano and F. Jean-Mary, *Journal of Physical Chemistry C*, 2010, **114**, 17460-17464.
25. J. R. Lakowicz, *Analytical biochemistry*, 2005, **337**, 171-194.
26. J. Qian and B. Tang, *Chem*, 2017, **3**, 56-91.
27. K. Miao and L. Wei, *ACS central science*, 2020, **6**, 478-486.
28. P. Jiang, M. Gan, S.-H. Yen and D. W. Dickson, *Frontiers in Molecular Neuroscience*, 2021, 234.
29. D. Wahyuningtyas, W. Chen, R. He, Y. Huang, C. Tsao, Y. He, C. Yu, P. Lu, Y. Chen, S. Wang, K. Ng, B. Chen, P. Wei, J. Shie, C. Kuo, Y. Sun and J. Huang, *Acs Applied Materials & Interfaces*, 2021, **13**, 60894-60906.
30. S. Li, J. He and Q.-H. Xu, *ACS omega*, 2019, **5**, 41-48.
31. P. LEE and D. MEISEL, *Journal of Physical Chemistry*, 1982, **86**, 3391-3395.
32. P. Borowicz, M. Latek, W. Rzodkiewicz, A. Łaszcz, A. Czerwinski and J. Ratajczak, *Advances in Natural Sciences: Nanoscience and Nanotechnology*, 2012, **3**, 045003.
33. G. Kresse and J. Hafner, *Physical review B*, 1993, **47**, 558.
34. G. Kresse and J. Hafner, *Physical Review B*, 1994, **49**, 14251.
35. G. Kresse and D. Joubert, *Physical review b*, 1999, **59**, 1758.
36. J. P. Perdew, K. Burke and M. Ernzerhof, *Physical review letters*, 1996, **77**, 3865.
37. S. Grimme, J. Antony, S. Ehrlich and H. Krieg, *The Journal of chemical physics*, 2010, **132**.
38. B. Mishra, D. Ghosh and B. P. Tripathi, *Journal of Catalysis*, 2022, **411**, 1-14.
39. A. Sharma, D. Kesamsetty, J. Debnath and K. S. Ghosh, *Journal of Molecular Liquids*, 2023, **372**, 121156.
40. L. Calzolai, F. Franchini, D. Gilliland and F. Rossi, *Nano Letters*, 2010, **10**, 3101-3105.
41. D. Zhang, O. Neumann, H. Wang, V. M. Yuwono, A. Barhoumi, M. Perham, J. D. Hartgerink, P. Wittung-Stafshede and N. J. Halas, *Nano letters*, 2009, **9**, 666-671.
42. A. Agrawal, I. Kriegel and D. Milliron, *Journal of Physical Chemistry C*, 2015, **119**, 6227-6238.
43. R. Han, W. Song, X. Wang, Z. Mao, X. Han and B. Zhao, *Physical Chemistry Chemical Physics*, 2018, **20**, 5666-5673.
44. D. Karthigeyan, S. Siddhanta, A. Kishore, S. Perumal, H. Agren, S. Sudevan, A. Bhat, K. Balasubramanyam, R. Subbegowda, T. Kundu and C. Narayana, *Proceedings of the National Academy of Sciences of the United States of America*, 2014, **111**, 10416-10421.
45. S. Siddhanta and C. Narayana, *Nanomaterials and Nanotechnology*, 2012, **2**.
46. S. Siddhanta, D. Karthigeyan, P. P. Kundu, T. K. Kundu and C. Narayana, *RSC advances*, 2013, **3**, 4221-4230.
47. J. Hu, R. S. Sheng and Z. San Xu, *Spectrochimica Acta Part A: Molecular and Biomolecular Spectroscopy*, 1995, **51**, 1087-1096.
48. G. Chandra, K. Ghosh, S. Dasgupta and A. Roy, *International Journal of Biological Macromolecules*, 2010, **47**, 361-365.
49. S. Schlucker, *Angewandte Chemie-International Edition*, 2014, **53**, 4756-4795.
50. S. Siddhanta, I. Barman and C. Narayana, *Soft Matter*, 2015, **11**, 7241-7249.
51. L. Fang, C. Huang, G. Shabir, J. Liang, Z. Liu and H. Zhang, *ACS Macro Letters*, 2019, **8**, 1605-1610.
52. H. Wang, B. Aydiner, Z. Seferoglu, F. Bures and J. Liu, *Dyes and Pigments*, 2022, **205**.
53. E. Zhao, J. W. Y. Lam, L. Meng, Y. Hong, H. Deng, G. Bai, X. Huang, J. Hao and B. Z. Tang, *Macromolecules*, 2015, **48**, 64-71.
54. C. Xing, J. W. Y. Lam, A. Qin, Y. Dong, M. Haeussler, W. Yang and B. Z. Tang.
55. S. C. Lee and R. H. Holm, *Chemical reviews*, 2004, **104**, 1135-1158.
56. Y. Shen, Z. An, H. Liu, B. Yang and Y. Zhang, *Angewandte Chemie*, 2023, **135**, e202214483.
57. L. Xue, F. Zou, Y. Zhao, X. Huang and Y. Qu, *Spectrochimica Acta Part a-Molecular and Biomolecular Spectroscopy*, 2012, **97**, 858-863.
58. M. Ganesan and P. Nagaraaj, *Organic Chemistry Frontiers*, 2020, **7**, 3792-3814.
59. L. Fang, C. Huang, G. Shabir, J. Liang, Z. Liu and H. Zhang, *Acs Macro Letters*, 2019, **8**, 1605-1610.
60. X. Wei, Y. Sun, C. Liu, Z. Li, X. Zou, D. Zhang, W. Zhang, J. Shi, X. Huang and Y. Li, *Sensors and Actuators B-Chemical*, 2021, **329**.
61. R. Bhattacharya, P. Mukherjee, Z. Xiong, A. Atala, S. Soker and D. Mukhopadhyay, *Nano Letters*, 2004, **4**, 2479-2481.
62. A. Shukla, S. Mukherjee, S. Sharma, V. Agrawal, K. V. R. Kishan and P. Guptasarma, *Archives of biochemistry and biophysics*, 2004, **428**, 144-153.
63. E. Lipiec, D. Perez-Guaita, J. Kaderli, B. Wood and R. Zenobi, *Angewandte Chemie-International Edition*, 2018, **57**, 8519-8524.